Identification of Pre-existing/Undetected Line-to-Line Faults in PV Array Based on Preturn ON/OFF Condition of the PV Inverter

Pradeep Kumar Boggarapu, *Student Member, IEEE*, Chakkarapani Manickam, Brad Lehman, *Fellow, IEEE*, Saravana Ilango Ganesan, *Senior Member, IEEE*, and Nagamani Chilakapati, *Senior Member, IEEE*

***Abstract*—A major challenge in a photovoltaic (PV) system is to identify the line-to-line faults that occurred under low irradiance conditions, during day-to-night/night-to-day transitions in the presence of blocking diodes. Due to active maximum power point tracker, these faults may not be identified and continue to be hidden even if the system returns to a high irradiance condition, since the magnitude of fault current may be less than the rating of the protection device (fuse). Those uncleared faults may subsequently lead to reduced peak output power, reliability issues, and may even cause fire risks. To address these issues, a method is proposed to identify the pre-existing/undetected faults using the transitory conditions that occur during the preturn ON/OFF condition of the PV inverter (checking mode). From these transitory conditions, the *I–V* curve of the PV array is exploited without the need for additional components or sensors. Additionally, there is no need to disconnect the PV array from the setup. Moreover, the local minima is tracked, to discriminate the faults and partial shading conditions. The proposed algorithm is tested on a small-scale grid-connected PV system and implemented in LabVIEW. The results demonstrate the efficacy of proposed algorithm in detecting the pre-existing/undetected faults.**

***Index Terms*—Existing/undetected faults, inverter preturn ON/OFF condition, *I–V* curve, local minima (LM), photovoltaic (PV) array.**

I. Introduction

AMONG the various renewable energy sources, solar photovoltaic (PV) energy has become increasingly implemented and predicted to reach the global PV generating capacity as 402 GW by the end of 2017 [1]. Nevertheless, the PV output power depends mainly on local weather condition, maximum power point tracking (MPPT) operation, aging of the PV panels, shading, and failures/faults in various components of the PV system. In fact, typical surveys of large PV systems have begun to document the significant energy losses due to PV faults and shading over the lifespan of an array, typically of the order of 4%–18% within a few years of operation [2]. This has led to increasing research on fault identification and detection for PV systems ([3]–[27], summarized below) with the goals to both increase energy yield of a PV system, as well as to improve safety and reliability.

The most prevalent PV array faults include such as line-to-line (LL) faults, line-to-ground (LG) faults, open-circuit (OC) faults, arc faults, and mismatch faults. Of these, LL and LG often involve massive fault currents and, therefore, lead to possible dangers, even fire hazards [3]. However, Zhao *et al.* [4] has recently narrated difficulties faced by the conventional protection devices in detecting LL and some LG faults under typical operating conditions. For example, when an LL fault occurs under high irradiance conditions, large fault currents are induced and, further, these faults are cleared by the installed overcurrent protection device (OCPD) (fuse). However, when the same fault occurs under low irradiance condition, the magnitude of fault current will be less than the rating of the fuse, so that it might not be cleared and continue to be obscure, even when the irradiance increases to a higher value. The reason is that the MPPT moves the operating point to a lower power faster than the operating time of fuse and might not be able to clear it. Similarly, faults occurring through high LL impedance or low percentage mismatch LL faults may also be undetectable. They will result in continuous decline in PV output power and may even pose fire risks. The fact that the PV array *I–V* characteristics under fault conditions are analogous to that under certain partial shading conditions (PSCs) makes it more difficult to detect the fault [5]. In summary, there is an urgent need to design a cost effective fault detection algorithm (FDA) which is capable of detecting the LL faults under low irradiance conditions and also able to discriminate the faults and PSC to avoid nuisance tripping. These are the objectives for this article.

In recent years, many fault detection methods have been proposed. Some approaches rely on time-domain responses of the PV system. Schirone *et al.* [6] investigated the faults, insulation failures, and broken cells using an offline scheme

Manuscript received December 6, 2019; revised February 20, 2020; accepted March 30, 2020. Date of publication April 15, 2020; date of current version July 20, 2020. This work was supported by the Ministry of Electronics and Information Technology, Government of India. Recommended for publication by Associate Editor V. Agarwal. *(Corresponding author: Saravana Ilango Ganesan.)*

Pradeep Kumar Boggarapu, Saravana Ilango Ganesan, and Nagamani Chilakapati are with the Department of Electrical and Electronics Engineering, National Institute of Technology, Tiruchirappalli 620015, India (e-mail: pradeep301327@gmail.com; gsilango@nitt.edu; cnmani@nitt.edu).

Chakkarapani Manickam is with the Department of Electrical and Electronics Engineering, Madanapalle Institute of Technology and Science, Madanapalle 517325, India (e-mail: chakra_nit@yahoo.com).

Brad Lehman is with the Department of Electrical and Computer Engineering, Northeastern University, Boston, MA 02115 USA (e-mail: lehman@ece.neu.edu).

Color versions of one or more of the figures in this article are available online at https://ieeexplore.ieee.org.

Digital Object Identifier 10.1109/TPEL.2020.2987856

called time domain reflectometry (TDR). In another study [7], spread spectrum TDR is employed to identify the faults, which is an online method. However, these methods require a signal generator and switching ON/OFF loads may leads to fallacious operation of the protection system.

Apart from the above technique, fault detection based on artificial intelligence and signal processing tools have been devised: local outlier detection [8], fuzzy inference system [9], k-nearest neighbors with nonparametric thresholds [10], artificial neural networks [11], and wavelets in conjunction with support vector machine technique [12]. These methods necessitate labeled data to tune the method and usually require additional sensors, which makes the protection system highly expensive. Similarly, wavelet packets in [13] whereas maximal overlap discrete wavelet transforms in [14] are used to identify and discriminate the faults and PSC based on the derived threshold values. Furthermore, for implementing these methods, advanced controllers are required, which is costly.

Another approach of fault detection is to compare differences between measured and estimated electrical quantities of PV system such as: PV output power and array losses [15], deviation in mean power, voltage, and duty cycle [16], fractional-order dynamic error computed from the PV output power degradation [17], digital twin approach [18], time series of normalized PV output power and sample entropy [19], based on the magnitudes and changing pattern of first and last module voltages in each string [20], by optimally placing the voltage sensors alone [21], while in [22] with the measurement of incoming and outgoing currents of each string, faults can be identified. Nonetheless, these methods require a large number of sensors, advanced controllers, and associated circuitry for integration. Thus, both the complexity and the overall cost of the protection system are increased.

There has been more recently an emerging approach for studying the faults based on estimating the *I–V* characteristics with a reduced number of measurement sensors, and this is similar to the objectives of this article. Normally, external equipment is needed to trace the *I–V* curve of the PV module/array namely using variable resistor load, capacitor, electronic load, and dc–dc converters [23]–[25]. These methods are both time-consuming and need external circuitry. Recently, Manjunath *et al.* [26] proposed a method to trace the *I–V* curve with reduced number of points, thereby reducing the time period and has begun to explore (as in this article) how a front-end dc–dc converter in an MPPT might be partially used to understand the operating points of the PV array. A recent study proposed a sensorless FDA to identify the faults; however, it requires further investigation under low irradiance condition [27].

From all the above literature, the FDA schemes appear to suffer from one or more of the following deficiencies such as 1) failure to detect the faults under low irradiance condition, 2) difficulty in segregating the faults and abrupt changes in the irradiation/PSC, 3) requiring additional sensors/hardware, 4) need voluminous labeled data, and 5) lack of compatibility.

To address the above issues, this article proposes the following research contributions.

1) A new *I–V* curve-based FDA is proposed. This approach utilizes the preturn ON/OFF condition of the grid-tied PV inverter without disturbing its normal operation. Because it utilizes the existing inverter circuitry, it does not require any additional equipment/sensors or additional cost.
2) Analytical derivation of the FDA is presented. Furthermore, it is demonstrated theoretically and in simulation how the proposed FDA can distinguish between LL faults and PSC by estimating the possible locations of "local minima" (LM) and comparing their locations with measured data.
3) A small-scale PV experimental prototype has been built with the ability to create both LL faults and PSC. The proposed FDA scheme has been validated by more than 96 experiment test cases.

In summary, this article helps in mitigating the open problem, i.e., how to identify and distinguish the pre-existing/unidentified PV array LL faults and PSC, without adding additional circuitry or noticeable costs. This has been an unsolved problem in the field of fault detection, until this research. Further, in the literature, no study has been discussed about, how to use the transients during the inverter preturn ON/OFF condition, for extracting the *I–V* curve of the PV array. Thus, the novelty of the proposed method is to extract the *I–V* curve of the PV without using additional equipment/sensors/skilled person and, that too, without the need to disconnect the PV from its normal operation. In addition to this, using LM concept, pre-existing/unidentified faults and PSC are identified and categorized.

The rest of this article is organized as follows. Section II describes the PV system and describes the consequences of existing faults due to MPPT operation. Section III illustrates the operation of PV inverter during preturn ON/OFF condition and the working of the proposed algorithm. Section IV depicts the experimental results to substantiate the efficacy of the proposed method. Finally, Section V concludes the article.

II. PV System and Consequence of Existing Array Faults on PV Output Power

A. Typical PV System and Faults in PV Array

The typical PV system depicted in Fig. 1 comprises of PV modules, traditional safeguard devices (ground fault protection device (GFPD) and OCPD-fuse), a dc–dc converter embedded with MPPT, and a grid-connected inverter. Additionally, in order to meet the input voltage and power ratings of the PV inverter, the PV modules (parameter specifications are listed in Table I) are arranged in series–parallel configuration, known as array. Furthermore, the bypass diode and the blocking diodes are connected to impede the hotspot formation [28] and flow of back-fed current into the faulty string, respectively. However, the usage of blocking diodes is optional in the PV installation and is not mandatory as per NEC in the USA [4]. Additionally, all the nonconducting metal parts and module frames are grounded to safeguard the equipment from the surges and faults and to avert electric shock.

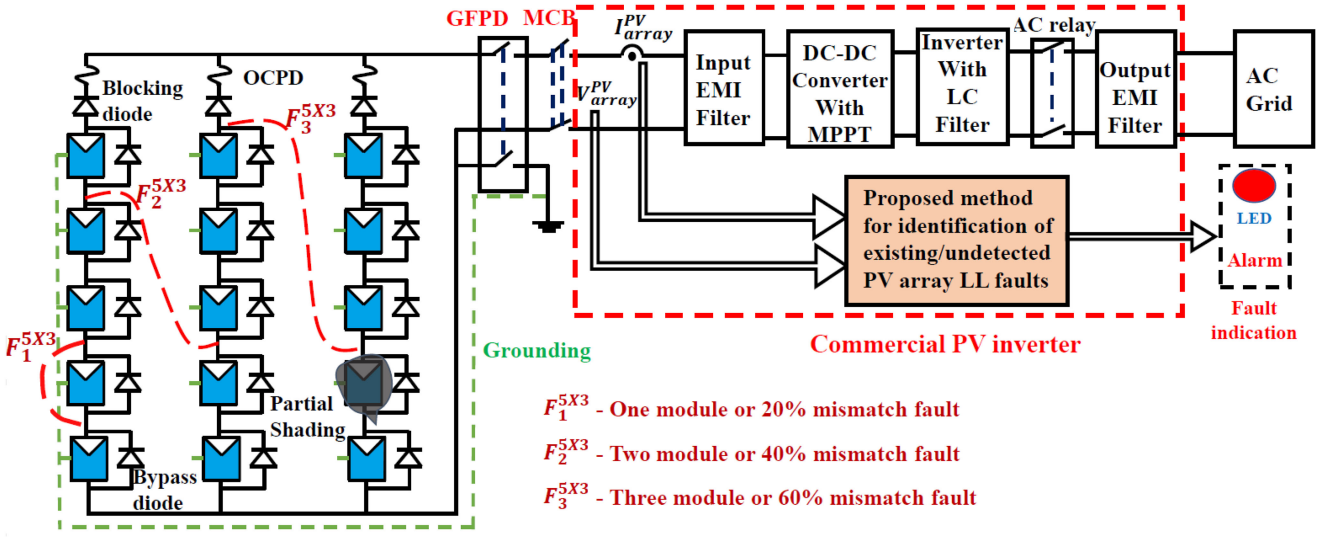

Fig. 1. Schematic diagram of a grid-tied PV system with proposed algorithm and illustration of various LL faults.

TABLE I
SPECIFICATIONS FOR A 100 Wp PV MODULE AND 5 × 3 PV ARRAY

Parameters	PV module rating	5 x 3 PV array rating
Peak Power	100 Wp	1500 Wp
Open circuit voltage	53.9 V	269.5 V
Short circuit current	3.14 A	9.42 A
Voltage at peak power	39.9 V	199.5 V
Current at peak power	2.51 A	7.53 A

The possible faults in the PV array are LL, LG, OC, and mismatch faults. Among these faults, LL and LG might involve a massive fault current, which may even cause fire risks. LL faults occur due to the formation of a short circuit between two discrete potential points within the same string or between the strings. Furthermore, when any one of the potential points is grounded, then it is referred as an LG fault. Therefore, LG fault is considered as a special case of LL fault. Thus, when the protection system detects the LL faults it means that it can identify the LG faults also [4], [15]. Furthermore, various LL faults are explicated in Fig. 1. From Fig. 1, $F_1^{5\times3}$ denotes LL fault with 20% mismatch (one among five modules is shorted) or LL fault with one module, likewise $F_2^{5\times3}$ and $F_3^{5\times3}$ indicates two-module (40% mismatch) and three-module (60% mismatch) LL faults, respectively. Furthermore, the severity of fault current depends on many factors such as percentage mismatch, location of fault, fault impedance, irradiance at the instant of fault, usage of blocking diodes, and MPPT operation.

B. Effect of MPPT on Pre-existing Faults and Its Consequences

For experimental demonstration, a 5 × 3 PV array configuration is considered and the corresponding PV output power

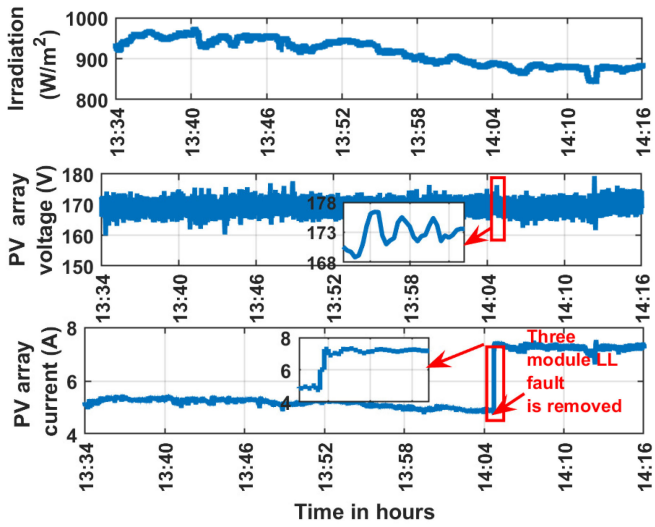

Fig. 2. Experimental data of the array voltage and current for the three-module existing LL fault in a 5 × 3 PV array configuration.

is connected to the grid through a 3-kW PV inverter shown in Fig. 1. An LL fault with 60% mismatch ($F_3^{5\times3}$) is created before the PV inverter starts sending power to the grid (existing fault). Once the inverter starts sending power to the grid, due to active MPPT, the PV array operates at reduced output power. Furthermore, the array output voltage and current appear to operate in a normal (unfaulted) condition (exemplified in Fig. 2). At the instant 14:04 h, the array fault was removed manually and at that moment, the PV array voltage ($V_{\rm arr}^{\rm PV}$) and current ($I_{\rm arr}^{\rm PV}$) start increasing (enlarged portion of the transient that occurred during the removal of fault is shown as subfigure in Fig. 2). The MPPT operation once again optimizes the PV output power and settles at a new operating point. From Fig. 2, it is implied that, before and after the removal of fault, the PV operating voltage is almost the same and further it is difficult to ascertain the existing

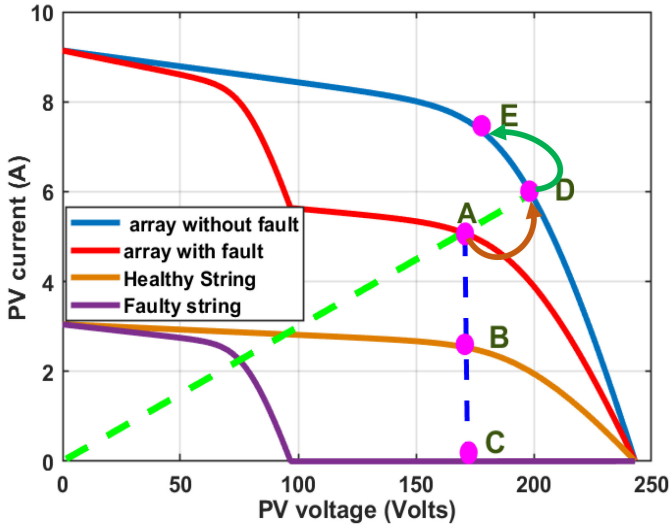

Fig. 3. Simulated *I–V* characteristics for a three module LL fault in a 5 × 3 PV array, at an irradiation of 892 W/m^2 and a temperature of 54.5 °C.

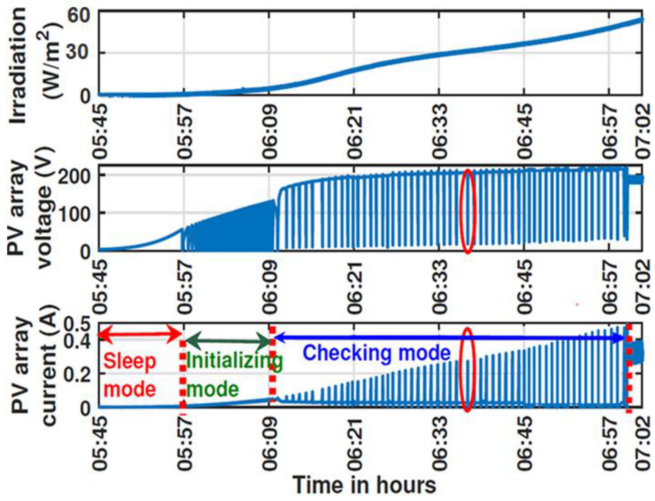

Fig. 4. Experimental data of the array current and voltage during the turn ON process of a grid-connected PV inverter when connected to a 5 × 3 PV array.

fault with the array current alone since array current may change due to environmental disturbance and shading. For better clarity, the change in the PV operating point is exemplified using the corresponding simulated *I–V* characteristics of the 5 × 3 PV array with and without fault at similar weather conditions, i.e., at an irradiation of 892 W/m^2 and a temperature of 54.5 °C (illustrated in Fig. 3).

From Fig. 3, it is clear that, under existing fault condition, due to active MPPT, the PV array operates at an operating point A (intersection point of the load line and the array *I–V* curve with fault) and the corresponding healthy string and faulty string operate at points B and C, respectively. From Fig. 3, it can be inferred that the faulty string is isolated from the power generation and there would be no backfed current due to the presence of blocking diodes, which makes the fault become blind spot. Furthermore, as soon as the LL fault is removed, instantly the MPP point shifts from A to D (slight increment in the array voltage and a sudden increase in the current is observed and is experimentally witnessed in Fig. 2). Due to MPPT operation, the PV array reaches to a new operating point E. At this new operating point, both the PV array and healthy string operate at almost same voltage as before the clearing of fault while the array current increases.

From the above discussion, it can be concluded that, when the inverter starts working with the existing fault, due to MPPT operation, the PV array operates at reduced output power and further, due to the presence of blocking diodes, there will be no backfed current to detect the fault. When the fault remains obscured for a long time, it may create fire risks. Thus, there is an exigent need to design an FDA that can ascertain and discriminate the existing faults from the normal conditions, which cannot be resolved by most of the existing FDAs.

III. Proposed Method

The basic idea of the proposed method is to trace the *I–V* curve of the PV, using the preturn ON/OFF condition of the grid-connected PV inverter. Furthermore, using LM concept, the proposed FDA detects and segregates the various LL faults based on the percentage mismatch. Key advantage of this approach is that it can be preprogrammed into existing MPPT inverters with no additional hardware costs.

A. Extraction of I–V Curve Using Preturn ON/OFF Condition of the Grid-Tied PV Inverter

Generalized block diagram for the commercially available PV grid-connected inverter (such as ABB, Huawei, and INVT) is depicted in Fig. 1 [29]–[31]. These commercial inverters comprise of dc filter, dc–dc converter, H-bridge inverter, ac relay (to synchronize the PV inverter to grid), and an ac electromagnetic interference (EMI) filter. Many of the inverter configurations use a boost converter to extract the peak power (using Perturb and Observe algorithm) from the PV array, which also acts as a controller in automatically connecting/disconnecting the PV inverter to the grid (turn ON/OFF condition of the PV inverter). For exemplifying the proposed method of fault detection, a 5 × 3 PV array experimental test-bed is considered and its output is coupled to an INVT iMars MG 3-KTL commercial inverter [32]. Furthermore, in practice, the typical turn ON process of a grid-connected PV inverter is explicated as follows.

From Fig. 4, during the early hours of the day, i.e., at time 05:45 h, the irradiation is zero W/m^2, and the PV inverter is in the OFF/shutdown/sleeping mode. Under such conditions, the PV inverter is isolated from the grid through ac contact relay, and its equivalent circuit is shown in Fig. 5. As the irradiation slowly increases, the PV array builds its voltage and the shunt capacitor voltage in the EMI filter follows the array voltage. When it goes beyond 60 V, the inverter enters into initializing mode. In this mode, the PV inverter frequently turns ON and OFF until the PV voltage reaches to 120 V. As soon as the PV voltage reaches 120 V (minimum start up voltage considered from the inverter data sheet [32]), the inverter is getting ready for sending power to the grid and this mode is known as "checking mode."

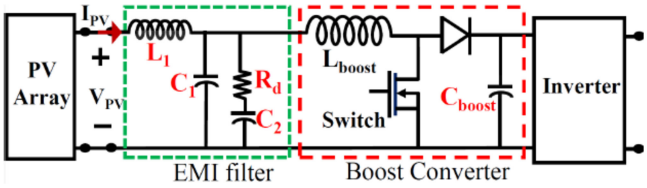

Fig. 5. Equivalent circuit of a PV inverter during preturn ON condition.

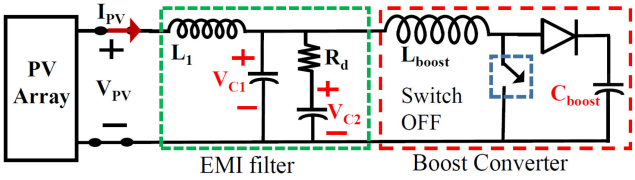

Fig. 6. Equivalent circuit of a PV connected inverter when the converter switch is in OFF condition.

In checking mode, the $V_{\text{arr}}^{\text{PV}}$ and $I_{\text{arr}}^{\text{PV}}$ fall and rise in transient until the magnitude of $I_{\text{arr}}^{\text{PV}}$ reaches 0.5 A, as shown in Fig. 4. Once the $I_{\text{arr}}^{\text{PV}}$ reaches 0.5 A, the inverter starts sending continuous power to the ac grid by closing the ac contact relay. Furthermore, during this inverter checking mode, the transients that occurred in the $I_{\text{arr}}^{\text{PV}}$ and $V_{\text{arr}}^{\text{PV}}$ are due to the operation of boost converter switch. The time period between the two consecutive transients is measured to be 54.93 s, which is much larger than the designed switching period of the boost converter, under normal running conditions of the inverter. Therefore, it is possible to measure the *I–V* characteristics of the PV during the checking mode, and analyzing the data can lead to FDA. Specifically, the operation during the checking mode can be described as follows.

1) Converter Switch Changes Its State From OFF to ON: During the inverter checking mode of operation, assume that the boost converter switch is in the OFF state for a long time (shown in Fig. 6). Under steady-state conditions

$$V_{C1} = V_{C2} = V_{\text{oc}}^{\text{array}} \text{ and} \tag{1}$$

$$I_{L1} = I_{C1} = I_{C2} = I_{\text{PV}} = 0 \tag{2}$$

where V_{C1}, V_{C2}—voltage across the capacitors C_1 and C_2, respectively, $V_{\text{oc}}^{\text{array}}$—OC voltage of the PV array, I_{C1}, I_{C2}—current through capacitors C_1 and C_2, respectively, and I_{L1}, $I_{L\text{boost}}$ represents the current through inductors L_1 and L_{boost}, respectively. From (1) and (2), it can be concluded that the PV is operating under OC conditions.

At the moment, when the switch is turned ON, the capacitors C_1 and C_2 are shorted through the boost inductor (L_{boost}) and the converter switch (illustrated in Fig. 7)

$$I_{C2} = \frac{V_{C1} - V_{C2}}{R_d} \tag{3}$$

$$V_{\text{PV}} = V_{C1} + V_{L1} \tag{4}$$

$$\text{KCL at node A, } I_{\text{PV}} - I_{C1} - I_{C2} = I_{L\text{boost}}. \tag{5}$$

Thus, these filter capacitors are discharging rapidly through the boost inductor (L_{boost}) and is explained using (3)–(5). As these transients are occurring at extremely low irradiance value, under such conditions, the magnitude of PV output current is very

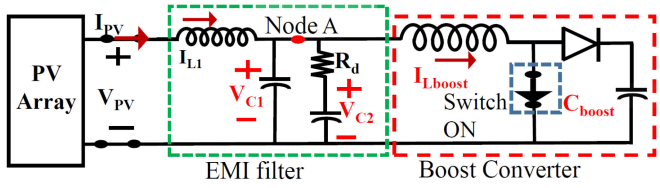

Fig. 7. Equivalent circuit of a PV-connected inverter when the converter switch is turned ON.

small and the rate of change of PV current is negligible. Thus, (4) becomes

$$V_{\text{PV}} \approx V_{C1}. \tag{6}$$

From (6), it can be inferred that as the V_{C1} changes, subsequently the PV operating point is changing. Furthermore, the magnitude of capacitor discharge current depends on the series resistance (R_d) and the difference of V_{C1} and V_{C2} values. As the series resistance (R_d) value is very small, even for a small difference in the capacitor voltages, capacitor supplies large current and hence V_{C1} and V_{C2} discharge rapidly. Under steady-state conditions, (5) becomes

$$I_{\text{Lboost}} \approx I_{\text{PV}} \approx I_{\text{SC}}, \text{ since } V_{\text{PV}} \approx V_{C1} \approx V_{C2} \approx 0\,V. \tag{7}$$

From (7), it can be inferred that the $I_{\text{arr}}^{\text{PV}}$ is approximately (ideally) equal to the PV array short-circuit current.

2) Converter Switch Changes Its State From ON to OFF: In the previous state, the PV array is operating near to short-circuit region. At this instant, when the converter switch is turned OFF (exemplified in Fig. 6), the capacitors C_1 and C_2 are slowly charging from the PV source, since the magnitude of PV source current is limited. Under steady-state conditions, the capacitors C_1 and C_2 are charged to $V_{\text{oc}}^{\text{array}}$ [replicates (1) and (2)].

From the above discussion, certain implications can be derived: 1) when the converter switch changes its state from OFF to ON, within a short period of time, the filter capacitors discharge rapidly. Subsequently, the PV array voltage rapidly drops from the OC voltage to approximately zero volts, and concurrently the array current increases sharply from zero Amperes to nearly short-circuit current and 2) when the converter switch changes from ON to OFF state, the filter capacitors (C_1 and C_2) slowly charge from zero volts to OC level ($V_{\text{oc}}^{\text{array}}$) through PV source, thereby resulting in a change of PV operating point from near short-circuit region to OC region. Therefore, the charging portion of the transitory condition (when the switch position changes from ON to OFF states) replicates the *I–V* curve of the PV array, since its voltage and current measurements theoretically sweep from near short-circuit to OC conditions.

Experimental plots of one of the checking mode transients (marked in Fig. 4) that occurred during the inverter preturn ON process are enlarged and illustrated in Fig. 8. In the plot, the array voltage drops from 207.3 V to a low value (18.8 V) and concurrently the array current increases rapidly to a magnitude of 0.3 A (close to the short-circuit current at that particular irradiance condition) because converter switch changes from OFF to ON state. Furthermore, when the converter switch changes from ON to OFF state, the array current gradually drops from

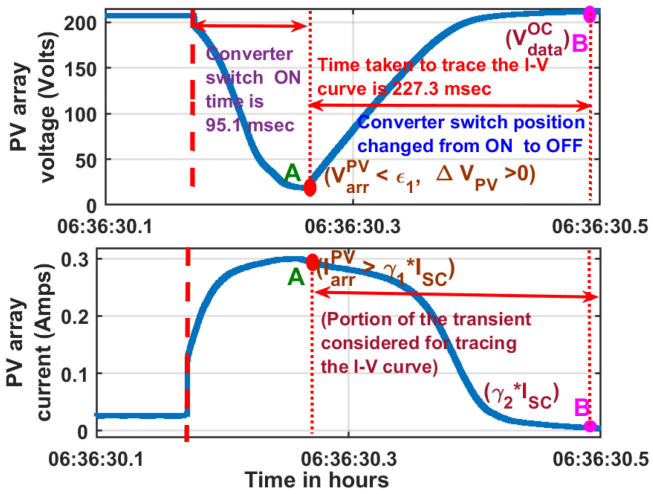

Fig. 8. Experimental result—enlarged portion of the transient that transited in $V_{\rm arr}^{\rm PV}$ and $I_{\rm arr}^{\rm PV}$, during the PV inverter checking mode.

TABLE II
TIME TAKEN TO REPEAT THE SCAN AND CONVERTER SWITCH ON/OFF TIMES DURING THE EXTRACTION OF *I–V* CURVE

Particulars of the event	Time in secs
Time period between the two consecutive transients (Switch OFF time)	54.93 secs
Converter switch ON time	95.1 msec
Time taken to trace the I-V curve	227.3 msec

0.3 A to a very low value (5 mA $\approx$ 0 A) while the array voltage rises from a low value (18.8 V) to 211.7 V (near to OC voltage at that particular irradiance condition). Thus, this charging portion of the transient replicates the *I–V* curve of the PV array. Furthermore, at this instant of time/irradiance, the converter switch ON time is 95.1 ms and the time taken for extracting the *I–V* curve is 227.3 ms depicted in Table II) and these time durations decrease with respect to the irradiation at which the transient occurs. Furthermore, during the inverter preturn ON condition, the maximum irradiation is observed as 58 W/m^2 (depicted in Fig. 4) and the corresponding maximum array short circuit ($I_{sc}^{\rm arr}$) is 0.546 A (=9.42*58/1000). Therefore, even when the converter switch is ON for a period of 95.1 ms, the inductor current may go up to a maximum of 0.546 A, which is very much less than the inductor rating. Thus, it may not cause any damage to the inductor.

The generalized procedure to trace the *I–V* curve of an S $\times$ T PV array (where S represents the number of series connected modules in a string and T indicates the number of such strings connected in parallel), during the checking mode of inverter operation is exemplified as follows.

1) The starting point of the *I–V* curve—"A" (near to short circuit operating point of PV shown in Fig. 8) is first identified, when the following conditions are fulfilled simultaneously:
   a) The array voltage falls below a small value, such as small percentage of $V_{oc}^{\rm array}$ at STC say ϵ_1 (= 12% of $V_{oc}^{\rm array}$ at STC). This condition is derived based on the drop in the array voltage during the inverter checking mode of operation. For the experimental test bed 5 $\times$ 3 grid-connected PV array, the array voltage drops to below 30 V at different instants of time as shown in Fig. 4.
   b) The array current should be greater than a certain percentage of its short-circuit current value, say γ_1 ($\approx$1% of array short-circuit current at STC and is considered as the peak magnitude of array current in the initializing mode, i.e., just before starting the checking mode of operation).
   c) $\Delta V_{\rm PV} > 0$ (where $\Delta V_{\rm PV} = V_{\rm arr}^{\rm PV}$(k)–$V_{\rm arr}^{\rm PV}$(k-1), represents change in the array voltage, used to identify the charging portion of the transient, i.e., increasing trend of the array voltage, which indicates the *I–V* curve of the PV array).
2) Recording the data: From the starting point "A" (depicted in Fig. 8), the array voltage and current are recorded until the instant "B," i.e., ending point of the *I–V* curve or OC voltage of the PV array (described in Fig. 8) is reached.
3) The ending point of the *I–V* curve: The ending point of the *I–V* curve (refers to instant B, described in Fig. 8) can be identified, when the array current falls below a very low value, say γ_2 ($<$ 0.5% of array short-circuit current at STC). This value may vary according to the resolution of the sensing element used in the inverter configuration. In practice, NI modules are used for sensing the array current and voltage with a sampling period of 0.2 ms and further these modules are more accurate and have high resolution. Thus, in this present experimental study, the γ_2 value is considered as 0.3% of array short-circuit current at STC. At this instant "B," the array voltage is close to the magnitude of array OC voltage at that particular irradiance condition. However, for identifying the instant "B", the array current rather than array voltage is the criterion considered, since the array OC voltage is constantly changing during the inverter checking mode of operation (PV voltage varies logarithmically according to the irradiance value and is illustrated in Fig. 4).

From this stored *I–V* curve data, the OC voltage of the PV array can be determined and is termed as $V_{\rm oc}^{\rm array}$. Furthermore, as these *I–V* curves are captured at discrete instants of time/irradiation values (6 to 58 W/m^2 depicted in Fig. 4), the magnitude of $V_{\rm oc}^{\rm array}$ is not unique for all the captured *I–V* curves. Thus, from the captured *I–V*, the first step is to determine the magnitude of $V_{\rm oc}^{\rm array}$ at that particular weather condition (irradiation and temperature). This experimentally determined $V_{\rm oc}^{\rm array}$ value is invoked for further investigations (LL faults and PSC), which indirectly includes the effect of the temperature and irradiation.

Furthermore, similar pattern of transients will occur in the $V_{\rm arr}^{\rm PV}$ and $I_{\rm arr}^{\rm PV}$ before the PV inverter enters into the sleep mode/turn OFF mode, i.e., preturn OFF condition, illustrated in Fig. 9. From Fig. 9, during the day to night transition, as the irradiation slowly falls and at time 05:57 h, the PV inverter enters into the checking mode. During this mode, the transients

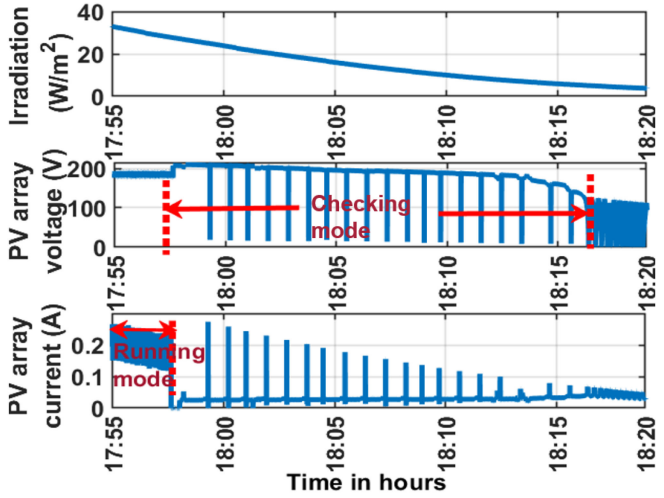

Fig. 9. Experimental results of the PV array current and voltage during the preturn OFF process of a grid-connected PV inverter.

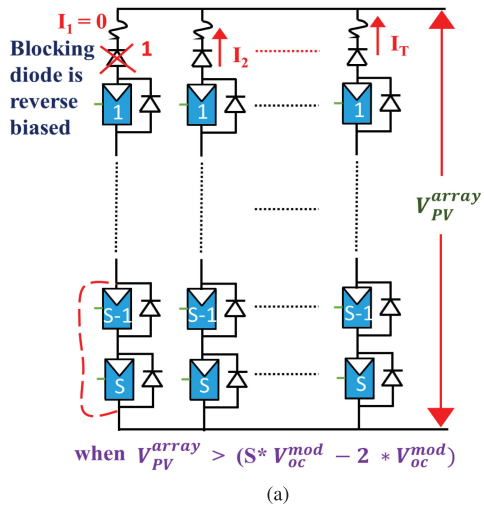

(a)

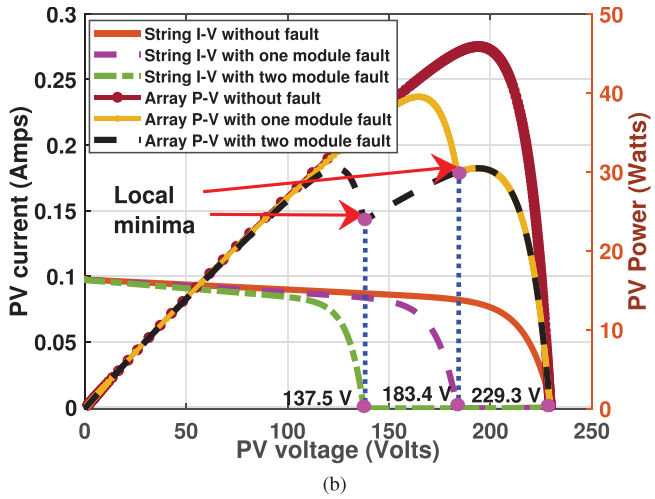

(b)

Fig. 10. (a) Two module LL fault in a S × T PV array installed with blocking diodes (b) under LL fault conditions, simulated I-V and P-V characteristics for a 5 × 3 PV array at an irradiation of 30 W/m^2.

will continue to transit in the $V_{\rm arr}^{\rm PV}$ and $I_{\rm arr}^{\rm PV}$, until the magnitude of $V_{\rm arr}^{\rm PV} > 120$ V (depicted in Fig. 9).

From the above investigation, it can be inferred that before connecting the PV inverter to the ac grid (during preturn ON)/before going to the sleep mode (preturn OFF), the transients that occur in the $V_{\rm arr}^{\rm PV}$ and $I_{\rm arr}^{\rm PV}$ are utilized for tracing the *I–V* curve of the PV array. Thus, the proposed method is an online method to trace the *I–V* curve of the PV array and it does not require any additional equipment or sensors. From the obtained *I–V* curve, pre-existing/undetected array faults and partial shading conditions (PSCs) are investigated.

B. LL Faults and Partial Shading Conditions

1) With Blocking Diodes: This section analytically demonstrates that LL faults can be detected using measurements during the inverter checking mode combined with some simple calculations that are derived below. Furthermore, using the calculations presented, it is possible to distinguish between LL faults and PSC, which had previously been a difficult challenge in PV fault detection.

Consider an S × T PV array installed with blocking diodes [depicted in Fig. 10(a)]. Under normal operating conditions, the blocking diodes will be forward biased and there exists no LM on the array P–V (Power versus Voltage) characteristics (or no step on the *I–V* curve), and the corresponding array voltage is expressed by using (8)

$$V_{\rm pv}^{\rm array} = V_1^{\rm mod} + V_2^{\rm mod} + \cdots + V_S^{\rm mod} = S.V_{\rm pv}^{\rm mod} \tag{8}$$

where $V_1^{\rm mod}$, $V_2^{\rm mod} \cdots V_S^{\rm mod}$ are the PV module voltages and assumed to be operating at the same voltage $V_{\rm PV}^{\rm mod}$. Furthermore, the array OC voltage is represented by (9)

$$V_{\rm oc}^{\rm array} = S.V_{\rm oc}^{\rm mod} \tag{9}$$

where $V_{\rm oc}^{\rm mod}$—represents module OC voltage. Under LL fault with "M" module mismatch [M = 1, 2 3, . . (S-1)], the faulty string OC voltage ($V_{\rm oc}^{f-{\rm str}}$) is reduced by M*$V_{\rm oc}^{\rm mod}$ while there is no change in the normal string OC voltage, i.e., S*$V_{\rm oc}^{\rm mod}$. Therefore, the expression for the faulty string OC voltage ($V_{\rm oc}^{f_{\rm str}}$) is given by (10)

$$V_{\rm oc}^{f-{\rm str}} = S * V_{\rm oc}^{\rm mod} - M * V_{\rm oc}^{\rm mod}. \tag{10}$$

At the instant, when the $V_{\rm pv}^{\rm array}$ is greater than $V_{\rm oc}^{f-{\rm str}}$, the normal strings try to feed the current into the faulty string, and then the blocking diode in the faulty string will be reverse biased (explicated using two module LL fault in an S × T PV array in Fig. 10(a)). Furthermore, at this instant of voltage, the corresponding faulty string will be open circuited, and subsequently, a step on the array *I–V* curve or an LM is observed on the power–voltage (P–V) curve. Thus, the generalized expression for the voltage at which the LM occurs ($V_{\rm LM}$) is expressed as follows:

$$V_{\rm LM}^{\rm fault} = V_{\rm oc}^{f-{\rm str}} = (1 - M/S) * S * V_{\rm oc}^{\rm mod}. \tag{11}$$

Furthermore, the magnitude of $V_{\rm LM}^{\rm fault}$ (11) is formulated in terms of array OC voltage as (12).

$$V_{\rm LM}^{\rm fault} = (1 - M/S) * V_{\rm oc}^{\rm array} \tag{12}$$

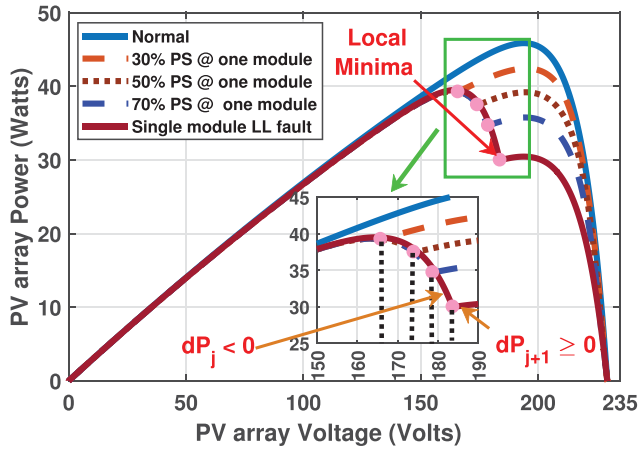

(a)

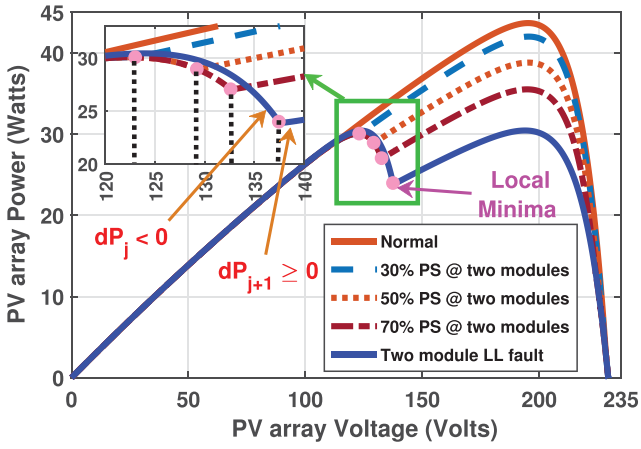

(b)

Fig. 11. Simulated P–V curves for the 5 × 3 thin film PV under PSCs and LL faults at (a) one module and (b) two modules.

where $V_{\rm oc}^{\rm array}$ indicates the measured OC of the PV array at that particular weather condition. From (12), it can be observed that for distinct module mismatch LL faults (M = 1, 2, ...), the $V_{\rm LM}^{\rm fault}$ occurs at distinct locations on the P–V curve. For a better clarity, the $V_{\rm LM}^{\rm fault}$ is computed in a 5 × 3 PV array. For one module [depicted in Fig. 10(b)], two module [depicted in Fig. 10(b)], three module and four module mismatch LL faults, the corresponding magnitudes of $V_{\rm LM}^{\rm fault}$ are 0.8* $V_{\rm oc}^{\rm array}$ (=183.4 V), 0.6* $V_{\rm oc}^{\rm array}$ (=137.6 V), 0.4* $V_{\rm oc}^{\rm array}$ (=91.7 V) and 0.2* $V_{\rm oc}^{\rm array}$ (=45.86 V), respectively. Therefore, to identify the LL faults, first determine the $V_{\rm oc}^{\rm array}$ and then actual $V_{\rm LM}$ values from the experimentally captured *I–V* curve during the inverter checking mode. Furthermore, the actual $V_{\rm LM}$ value is determined by computing the change in the array power ($dP_j = P_{j+1} - P_j$) and with the fulfillment of conditions ($\mathrm{dP}_j < 0, \mathrm{d}_{j+1} \geq 0$, illustrated in Fig. 11). Then, $V_{\rm LM}^{\rm fault}$ is computed as in (12) and compared with the measured $V_{\rm LM}$ (actual $V_{\rm LM}$). For a value of "M," when both the magnitudes (actual $V_{\rm LM}$ and computed $V_{\rm LM}^{\rm fault}$) are within the tolerance of approximately 1% of array OC voltage (≈2.69 V, in case of 5 × 3 PV array), then it indicates that an LL fault with "M" module mismatch has occurred, otherwise partial shading has occurred in the PV array. The tolerance 1% of array OC voltage is considered to include the deviation of actual $V_{\rm LM}$ from the computed $V_{\rm LM}^{\rm fault}$ location due to measurement errors.

TABLE III
COMPARING ACTUAL $V_{\rm LM}$ AND COMPUTED $V_{\rm LM}^{\rm fault}$ VALUES DERIVED FROM THE SIMULATED P–V CURVES AT AN IRRADIANCE OF 30 W/m^2 AND A TEMPERATURE OF 25 °C

%shading/ fault	__ occurs at one module		__ occurs at two module	
	Actual $V_{\rm LM}$	Computed $V_{\rm LM}^{\rm fault}$ (M = 1)	Actual $V_{\rm LM}$	Computed $V_{\rm LM}^{\rm fault}$ (M = 2)
30	165.7	183.4	123	137.6
50	173.9	183.4	129.2	137.6
70	178.6	183.4	132.6	137.6
Fault	183.6	183.4	137.4	137.6

In addition to the LL fault condition, under PSC, an LM occurs due to the conduction of bypass diode (described in [33]). However, the location of $V_{\rm LM}$ under PSC will be at distinct voltages lower than the magnitude of $V_{\rm LM}^{\rm fault}$ in (12). To illustrate this, a 5 × 3 PV array is chosen and is simulated in MATLAB/Simulink [34], [35] at a low irradiation of 30 W/m^2 and a temperature of 25 °C. Furthermore, the P–V curves under PSC with distinct %shadings and LL faults at one and two modules are plotted in Fig. 11(a) and (b), respectively, and the corresponding actual $V_{\rm LM}$ values are tabulated in Table III. Additionally, the computed $V_{\rm LM}^{\rm fault}$ [using (12)] for one module (M = 1) and two module (M = 2) mismatch LL faults are 183.4 V (=0.8 * 229.3 V) and 137.6 V (=0.6 * 229.3 V), respectively, listed in Table III.

From Table III and Fig. 11, it can be concluded that the magnitude of $V_{\rm LM}$ under PSC occurs at lower voltages and will approach the $V_{\rm LM}$ under LL fault condition, only at 100% shading condition. In practice, 100% shading occurs only when the PV panel is fully covered with an opaque object, which is an exceptional case and is treated as an LL fault by the proposed FDA. Since the *I–V* curve data are known and recorded (explicated in Section III-A), the proposed FDA is able to identify and discriminate the LL faults and PSC by comparing the actual $V_{\rm LM}$ with the computed $V_{\rm LM}^{\rm fault}$ value using (12). Extensive simulations in MATLAB/Simulink have been performed to validate the proposed method in distinguishing the LL faults and PSCs:

1) A total of 135 partial shading simulations at distinct irradiance values of 30, 40, and 50 W/m^2 with the combinations of 10%, 30%, 50%, 60%, 70%, and 80% shading at one module, two module, and three modules, respectively, and in the temperature range of 20 °C–35 °C in steps of 5 °C temperature variation.
2) More than 27 discrete % discrete mismatch LL faults (one module, two modules, three modules, and four modules) are simulated at distinct irradiance values of 30, 40, and 50 W/m^2 and at various operating temperatures such as 20, 25, 30, and 35 °C.

From the above simulations, it can be concluded that, with the tolerance of 1% of array OC voltage at STC, the LL faults and

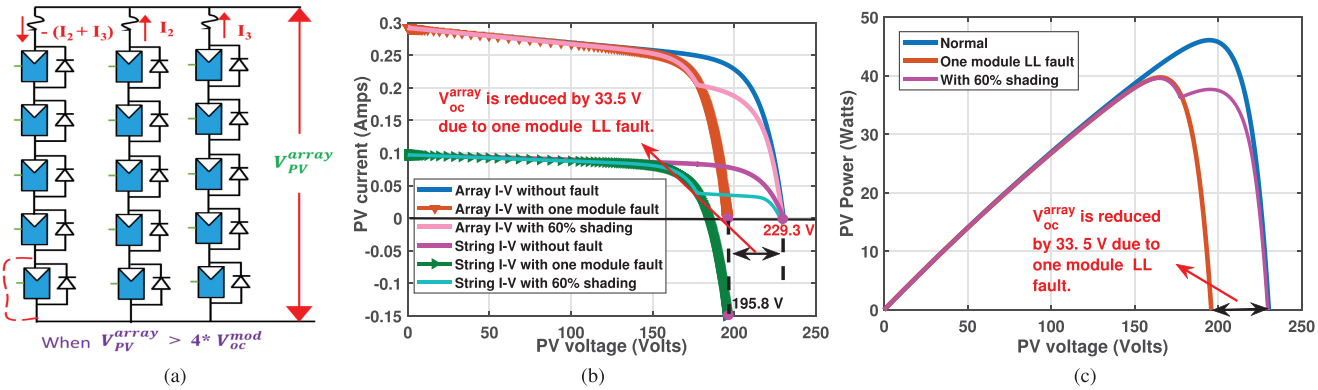

Fig. 12. Under LL fault conditions, (a) S × T PV array without blocking diodes, (b) Simulated string and array *I–V* characteristics for a 5 × 3 PV array at an irradiation of 30 W/m^2, (c) Simulated array P–V characteristics for a 5 × 3 PV array, at an irradiation of 30 W/m^2.

PSC are successfully identified. Therefore, when the difference between the actual $V_{\rm LM}$ and computed $V_{\rm LM}^{\rm fault}$ (12) values is within the tolerance of 1% of array OC voltage at STC (= 2.69 V, in case of 5 × 3 PV array), then it indicates an LL fault has occurred, otherwise, PSC has occurred in the PV array.

2) Without Blocking Diodes: As per the NEC standards in the USA [4], blocking diodes are not installed in the PV system. LL faults and PSC are investigated using an example; a 5 × 3 PV array without blocking diodes [depicted in Fig. 12(a)] is simulated in MATLAB/Simulink at an irradiation of 30 W/m^2 and a temperature of 25 °C. Under normal operating conditions, the array OC voltage is 229.3 V. When an LL fault with one module mismatch occurs, the array OC voltage is reduced to 195.8 V, which is approximately reduced by half of the $V_{\rm oc}^{\rm mod}$ at STC [shown in Fig. 12(b)], which is a significant reduction in the $V_{\rm oc}^{\rm array}$. This is because, when the $V_{\rm pv}^{\rm array}$ is greater than 4* $V_{\rm oc}^{\rm mod}$, the normal strings supply backfed current into the faulty string. Furthermore, the healthy modules in the faulty string operate in the fourth quadrant (operating voltage is $> V_{\rm oc}^{\rm mod}$) and subsequently the faulty string acts as a load for the other normal strings. However, under PSC, there exists an LM due to the conduction of bypass diode, and there is no reduction in the $V_{\rm oc}^{\rm array}$ [shown in Fig. 12(c)]. Therefore, it is easy to identify and discriminate the LL faults and PSCs by monitoring the OC voltage of the PV array.

Thus, using the proposed method of extraction of *I–V* curve, LL faults and PSC are identified and differentiated irrespective of the PV system installed with/without blocking diodes.

Therefore, the generalized algorithm for identifying the existing/undetected LL faults in an S × T PV array installed with blocking diodes can follow the formal algorithm below.

C. Algorithm for Detection of Faults in PV Array

In this article, the only inputs fed to the proposed FDA are the PV array voltage and current. Furthermore, the irradiance data shown in Figs. 4 and 9 are just to reveal that the magnitude of irradiance is very low (less than 60 W/m^2) during the inverter preturn ON/OFF conditions and is not fed as an input to the proposed FDA.

Generalized flowchart for 1) measuring/recording the *I–V* curve, and then 2) detecting and segregating the faults and PSCs is presented in Fig. 13.

Step 1: The variable "FS" is initialized to zero, i.e., FS = 0, where FS indicates fault status.

Step 2: The PV array current and voltage are sampled at a frequency of f_s (say 5 kHz) and the corresponding $\Delta V_{\rm PV}$ is computed. The variable used for counting the number of samples is initialized (k = 1).

Step 3: The starting point "A" is identified, when the three conditions explicated in the earlier Sections III-A(2) are satisfied.

Step 4: From this starting point A, the array voltage and current are recorded until the array current drops to a value γ_2 (described in Section III-A) and then the algorithm starts executing from the Step 6.

Step 5: If the starting point is not yet identified, then the sample count is incremented by 1 and Step 3 will be repeated until k = f_s (say $f_s = 5000$). If k > f_s, Step 2 is repeated.

Step 6: This recorded data represent the *I–V* curve of the PV array and from this data, the OC voltage ($V_{\rm oc}^{\rm array}$), PV output power [$P_j = V_{\rm arr}^{\rm PV}$ (j)* $I_{\rm arr}^{\rm PV}$(j)] and length of the stored data (say R) is computed. Furthermore, the change in the PV output power (dP_j) is calculated as follows:

$$dP_j = (P_j - P_{j-1}). \tag{13}$$

Furthermore, the count for the LM and recorded data are initialized (LM = 0 and j = 1).

Step 7: If the conditions ($dP_j < 0$ and $dP_{j+1} \geq 0$) are satisfied, then LM is incremented by 1 and the $V_{\rm LM}$ (actual value) is recorded.

Step 8: The data count (j) is incremented by 1 and Step 7 is repeated, until all the recorded data are verified.

Step 9: If LM is equal to zero, then it indicates normal condition and Step 2 is repeated.

Step 10: The actual $V_{\rm LM}$ (determined from the captured *I–V* curve) is compared with the magnitudes of computed $V_{\rm LM}^{\rm fault}$ for M = 1, 2,... (S-1), using (12).

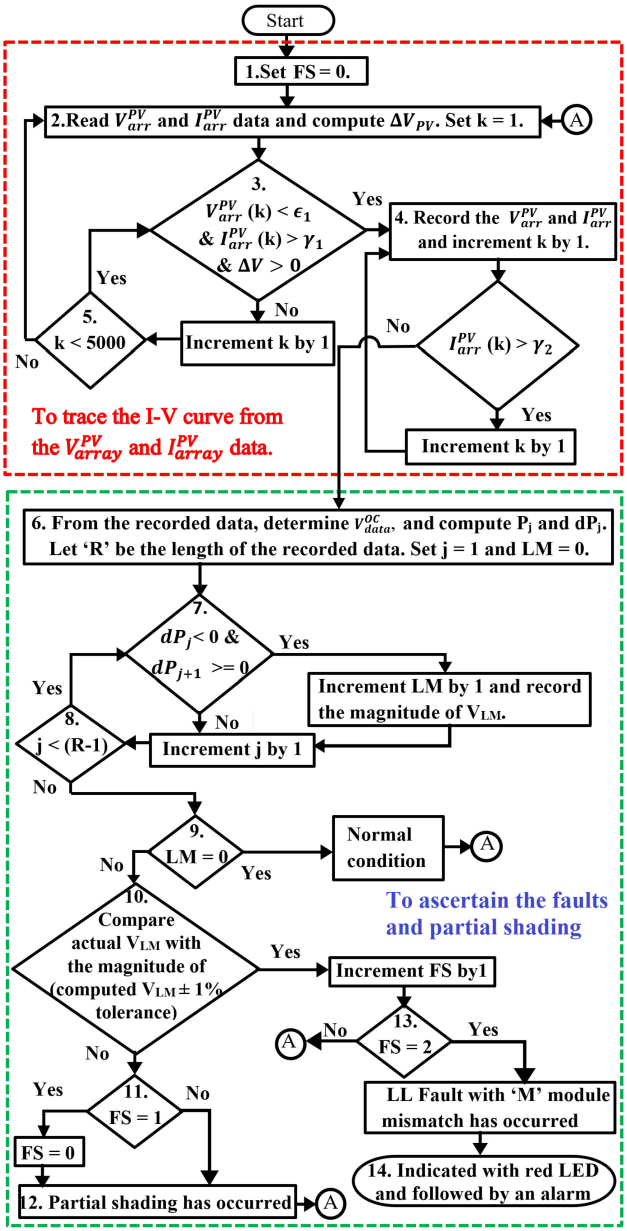

Fig. 13. Flowchart for the proposed FDA.

When both the values (computed $V_{\mathrm{LM}}^{\mathrm{fault}}$ for "M" value and actual V_{LM}) are within a tolerance band of approximately 1% of $V_{\mathrm{oc}}^{\mathrm{array}}$ at STC, then FS is incremented by 1 and the execution starts from Step 13.

Step 11: If FS is equal to one, then set FS = 0.

Step 12: Partial shading has occurred in the PV array and Step 2 is repeated.

Step 13: If FS = 2, then it indicates an LL fault with "M" module mismatch has occurred in the PV array, else Step 2 is repeated.

Step 14: An occurrence of LL fault is indicated by lightening up of a red LED followed by an alarm. Furthermore, the alarm can be reset only after the removal of LL fault.

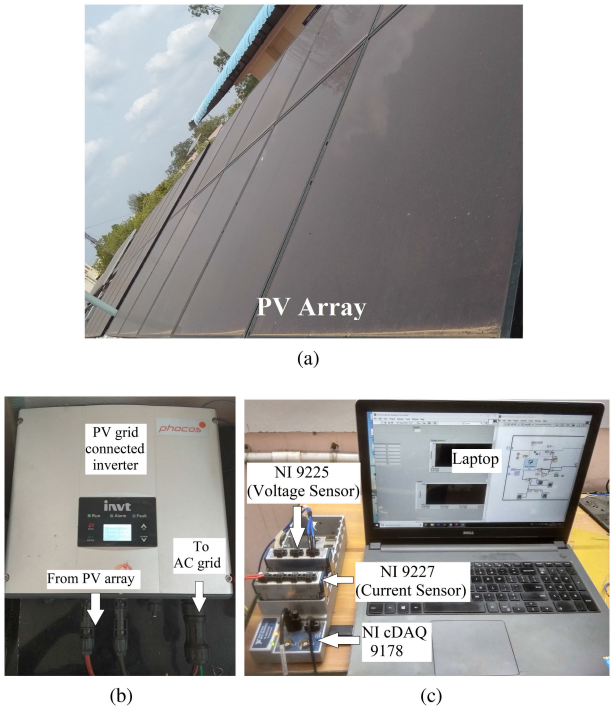

Fig. 14. Experimental setup, (a) PV array, (b) PV grid-connected inverter, (c) Data acquisition system using NI modules and computing device.

IV. Experimental Results and Discussions

A. Experimental Setup

To assess the performance of the proposed method, an experimental setup is configured (shown in Fig. 14), which consists of 5 × 3 Thin film PV array, 3 kW PV grid-connected inverter (iMars MG-3 KTL [32]), data acquisition system using NI devices, and a personal computer. For clear demonstration, the proposed algorithm is implemented in the LabVIEW and the only inputs fed to the proposed algorithm are $V_{\mathrm{arr}}^{\mathrm{PV}}$ and $I_{\mathrm{arr}}^{\mathrm{PV}}$ sampled at a frequency of 5 kHz using NI9225 and NI9227, respectively. However, all the conventional grid-tied PV inverters are readily equipped with the voltage and current sensors at their input side. Furthermore, the inverters have their own microcontrollers for MPPT and, therefore, the proposed method can easily be incorporated inside the inverter, without additional hardware/sensors costs.

In practice, the input signals ($V_{\mathrm{arr}}^{\mathrm{PV}}$ and $I_{\mathrm{arr}}^{\mathrm{PV}}$) are averaged with a window width of three samples, to fade out the effect of noise. From the smooth voltage and current signals, PV output power is determined. Therefore, the P–V curve will be smooth, even in a noisy environment. As the sampling frequency is 5 kHz, the averaging technique does not show much impact on the magnitude of actual V_{LM}. Furthermore, to ensure the effectiveness of the proposed method, the algorithm is supposed to check with the two consecutive *I–V* curves.

B. Identification of Existing/Undetected LL Faults

In this section, the efficacy of the proposed algorithm is experimentally tested in identifying the two module mismatch

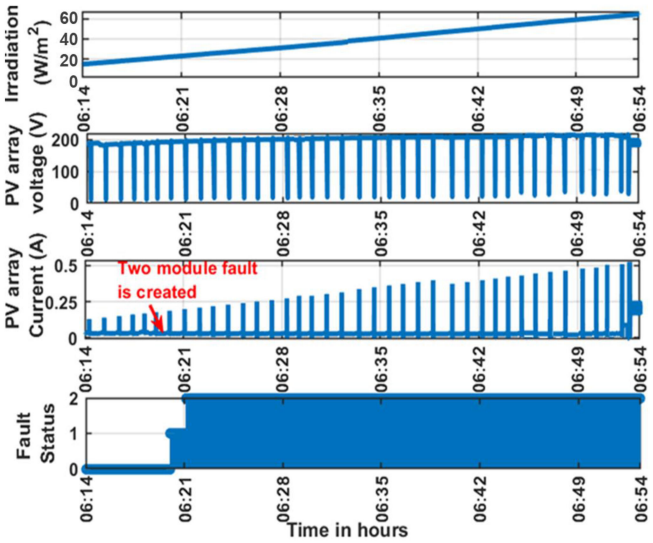

Fig. 15. Experimental results for the two-module fault occurred under extremely low irradiance condition.

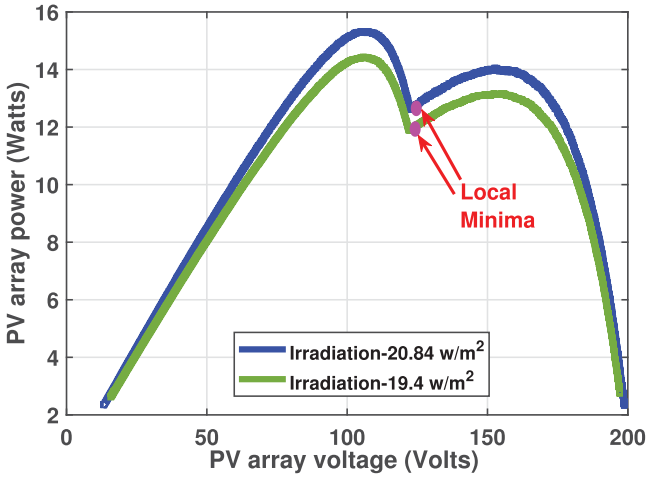

Fig. 16. Experimental results—P–V curves for the two-module fault occurred under extremely low irradiance condition.

fault occurred under extremely low irradiance condition. During the early hours of the day, i.e., at time 06:19 h, a two-module mismatch fault is created manually (depicted in Fig. 15) and, at that instant, the irradiance value is 18.36 W/m^2, which is an extremely low irradiance condition. After the three conditions of Step 3 are satisfied, the data are recorded until the Step 4 condition is satisfied. From these recorded data, for the first two transients from the occurrence of fault (shown in Fig. 15), the corresponding P–V curves are plotted in Fig. 16. Furthermore, from each *I–V* curve, magnitude of $V_{\rm oc}^{\rm array}$, computed $V_{\rm LM}^{\rm fault}$ [using (12)] and actual $V_{\rm LM}$ values are determined and listed in Table IV. From Table IV, for the first *I–V* curve (whose $V_{\rm oc}^{\rm array}$ is 198.1 V), it is clear that the difference between the actual $V_{\rm LM}$ and the computed $V_{\rm LM}^{\rm fault}$ value is less than the tolerance of 1% array OC voltage at STC (<2.69 V) satisfies the criteria to ascertain the fault; thus, the fault status value is changed from zero to one at 06:20 h (illustrated in Fig. 15). Similarly, for the

TABLE IV
COMPARING ACTUAL $V_{\rm LM}$ AND COMPUTED $V_{\rm LM}^{\rm fault}$ VALUES DERIVED FROM THE EXPERIMENTALLY OBTAINED *I–V* CURVES FOR A TWO-MODULE LL FAULT

Fault	Magnitude of $V_{\rm OC}^{\rm array}$ (V)	Computed $V_{\rm LM}^{\rm fault}$ (V) (M = 2)	Actual $V_{\rm LM}$
F_2^{5X3}	198.1 V	118.9 V	120.6 V
F_2^{5X3}	198.7 V	119.2 V	121.2 V

TABLE V
COMPARING ACTUAL $V_{\rm LM}$ AND COMPUTED $V_{\rm LM}^{\rm fault}$ VALUES DERIVED FROM THE EXPERIMENTALLY OBTAINED *I–V* CURVES

% Shading/ fault	Magnitude of $V_{\rm OC}^{\rm array}$	Computed $V_{\rm LM}^{\rm fault}$ (M = 1)	Actual $V_{\rm LM}$
26%	219.75 V	175.8 V	149.7 V
45%	214.1 V	171.3 V	158.8 V
61%	214.25 V	171.4 V	165.5 V
F_1^{5X3}-fault	215.5 V	172.4 V	172.2 V

next transient, i.e., at 06:21 h, the difference in both the values (actual $V_{\rm LM}$ and computed $V_{\rm LM}^{\rm fault}$) is less than the 1% tolerance value (shown in Table IV), then fault status value is incremented by 1. Therefore, after the two successive *I–V* curves, the fault status is changed to 2 (shown in Fig. 15), which indicates an LL fault has occurred and the red LED alarm is illuminated.

C. Discrimination of Faults and PSCs

To verify that the proposed FDA can distinguish between the LL faults and PSCs, an LL fault with one module mismatch and various percentage shadings are applied separately. As the proposed method is executing during the preturn ON/OFF condition of the inverter, i.e., under extremely low irradiation (< 60 W/m^2, depicted in Fig. 4), the effect of shadowing caused by the nearby buildings and trees are negligible. Moreover, to know the possible depth of shading that occur in the PV array during the inverter turn ON condition, a plank is placed at different distances from the PV module. The effect of shadow is significant, when the plank is less than half feet distance and the corresponding %shading is observed as 22.6. Therefore, for the verification of the proposed algorithm, a rare possibility of 61% shading (almost three times that of the shading observed in real time, which is a worst case and is achieved by placing eight layers of thick polythene sheet) is considered. Therefore, partial shading is created at one module by covering the PV panel with discrete multiple layers of polythene cover say 26% (2-layers of thick polythene sheets), 45% (4-layer), and 61% shading (8-layer) at different instants of time/irradiance values during the inverting checking mode of operation. The respective P–V characteristics are depicted in Fig. 17, with Table V indicating the magnitudes of $V_{\rm oc}^{\rm array}$ and actual $V_{\rm LM}$ values.

As explained earlier in Section III-B that, under LL fault with "M" number of modules shorted, the $V_{\rm LM}^{\rm fault}$ occurs at $V_{\rm oc}^{\rm array}$ *(1−M/S) V (in the present array configuration, S = 5 and M = 1, 2, 3, 4) and thus for the one module LL fault, the estimated

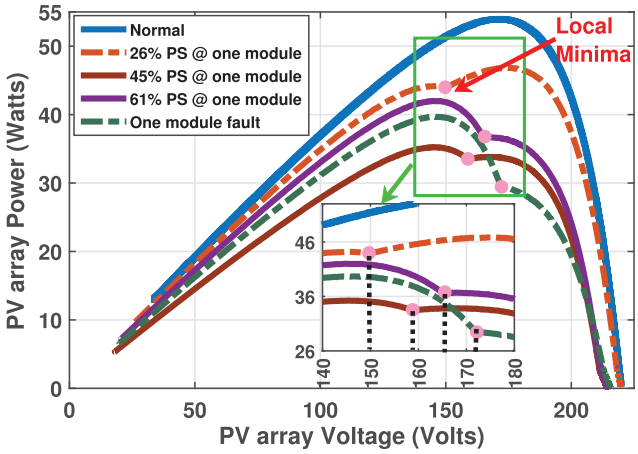

Fig. 17. Experimental P–V curves captured during the inverter checking mode, for one module mismatch LL fault and for various %shadings.

$V_{\rm LM}$ occurs at 0.8 * $V_{\rm oc}^{\rm array}$. From the experimentally determined magnitudes of $V_{\rm oc}^{\rm array}$, the $V_{\rm LM}^{\rm fault}$ values are computed using (12), and listed in Table V. From Table V, it can be concluded that for all the PSC, the actual $V_{\rm LM}$ is substantially deviated from the computed $V_{\rm LM}^{\rm fault}$, whereas for the one module fault (F_1^{5X3}), the actual $V_{\rm LM}$ and the computed $V_{\rm LM}^{\rm fault}$ are almost the same (negligible error of 0.2 V, within the tolerance of 1% of $V_{\rm oc}^{\rm array}$ at STC). Thus, the proposed algorithm successfully identifies and differentiates the faults and PSC. Similarly, the other percentage mismatch faults can be easily differentiated by using the LM concept. Furthermore, the proposed method has been experimentally tested and validated for more than 96 cases with the following combinations;

Case i): one-module, two-module, and three-module mismatch faults at different irradiance values in the range of 15–40 W/m^2;

Case ii): various partial shading tests with the shading cases of 11%, 26%, 32%, 45%, and 61% at one module, two modules, and three modules, respectively;

Case iii): discrete partial shading tests and faults in the temperature range of 20.2–33.6 °C, since during the inverter preturn ON/OFF condition (early hours of the day, i.e., before 07:00 am and late hours of the day, i.e., after 06:00 pm), the temperature is low.

For the above cases, the proposed FDA accurately identified the faults and none of the shading case is detected as a fault. In addition to this, the presence of cell breakage/light-induced degradation/soiled modules in a PV array [36]–[38], the PV array characteristics are similar to that under PSC. Furthermore, due to increase in series resistance (R_{se}), slope of the *I–V* curve near to OC voltage region will change and while due to decrease in shunt resistance ($R_{\rm sh}$), the slope of the *I–V* curve near to short-circuit current region ($I_{\rm sc}$) will be affected. Similarly, due to potential-induced degradation, there will be a change in the slope of the *I–V* curve near to $I_{\rm sc}$. Therefore, due to changes in $R_{\rm sh}/R_{se}$ or both, maximum power and fill factor will be subjected to change [39], [40]. Thus, due to the presence of either $R_{\rm sh}/R_{se}$ affected modules, no LM exists on the P–V curve. Therefore, because of the existence of these scenario PV modules in the PV array, the proposed FDA will not be detected as a fault condition.

D. Remark

The proposed FDA can also be used to detect and distinguish the LL faults and PSC in conditions other than low irradiance or preturn ON/OFF. At any instant of time/irradiation, the *I–V* curve of the PV array can be traced just by disengaging and coupling the PV array to the inverter through the connected miniature circuit breaker (MCB) between the PV array and inverter (shown in Fig. 1). After recording the *I–V* data, the same algorithm can be applied to identify and discriminate LL faults and PSCs. The disadvantage of the approach would be the loss of energy occurring during the disengaging of the inverter. On the other hand, it does allow for quick determination of whether an LL fault occurred during higher irradiance conditions. Furthermore, without additional sensors/labeled data, the proposed FDA has the ability to distinguish LL faults and PSCs.

V. Conclusion

This article has proposed a new method to ascertain the various existing/undetected array LL faults in a PV system installed with blocking diodes. The concept behind this method is to extract the *I–V* curve from the transitory conditions that emerged in the PV array voltage and current, during the inverter preturn ON/OFF condition. Moreover, using an LM concept, LL faults are segregated with respect to percentage mismatch and further clearly discriminated the PSCs. The analytical reasons for the ability to detect the faults have been explicated. Furthermore, the proposed approach is validated with the simulation and experimental results. An alarm (red LED indicator) has been used to indicate the fault condition and this approach leads to the ability to use the same alarm signal to either mechanically or electrically disengage these faults. This allows improved safety, reliability, and may even increase energy yield since the fault can be cleared.

In summary, the proposed method works for both the PV systems installed with and without blocking diodes, and it is very attractive for large PV plants since the measurements and computation would be inside the existing inverters itself. Furthermore, it does not require any additional hardware/sensors/labeled data and obviates the need for a dedicated protection system for the PV plant.

Acknowledgment

This work was performed at the National Institute of Technology, Tiruchirappalli, India, funded through Young Faculty Research Fellowship under the DeitY Visvesvaraya Ph.D. scheme.

References

[1] M. Eckhart, M. El-Ashry, D. Hales, K. Hamilton, and P. Rae, "Renewables 2018 Global Status Report," *Renewable Energy Policy Network*, 2018.

[2] S. Firth, K. Lomas, and S. Rees, "A simple model of PV system performance and its use in fault detection," *Solar Energy*, vol. 84, no. 4, pp. 624–635, 2010.

[3] B. Brooks, "The bakersfield fire: A lesson in ground-fault protection," *Solar Pro Mag.*, vol. 4, pp. 62–70, 2011.

[4] Y. Zhao, J. de Palma, J. Mosesian, R. Lyons, and B. Lehman, "Line-line fault analysis and protection challenges in solar photovoltaic arrays," *IEEE Trans. Ind. Electron.*, vol. 60, no. 9, pp. 3784–3795, Sep. 2013.
[5] R. Hariharan, M. Chakkarapani, and G. S. Ilango, "Challenges in the detection of line-line faults in PV arrays due to partial shading," in *Proc. Int. Conf. Energy Efficient Technologies Sustain.*, Apr. 2016, pp. 23–27.
[6] L. Schirone, F. P. Califano, U. Moschella, and U. Rocca, "Fault finding in a 1 mw photovoltaic plant by reflectometry," in *Proc. IEEE 1st World Conf. Photovolt. Energy Convers.*, Dec. 1994, vol. 1, pp. 846–849.
[7] S. Roy, M. K. Alam, F. Khan, J. Johnson, and J. Flicker, "An irradiance-independent, robust ground-fault detection scheme for PV arrays based on spread spectrum time-domain reflectometry (SSTDR)," *IEEE Trans. Power Electron.*, vol. 33, no. 8, pp. 7046–7057, Aug. 2018.
[8] Y. Zhao, B. Lehman, R. Ball, J. Mosesian, and J. de Palma, "Outlier detection rules for fault detection in solar photovoltaic arrays," in *Proc. 28th Annu. IEEE Appl. Power Electron. Conf. Expo.*, Mar. 2013, pp. 2913–2920.
[9] Z. Yi and A. H. Etemadi, "Fault detection for photovoltaic systems based on multi-resolution signal decomposition and fuzzy inference systems," *IEEE Trans. Smart Grid*, vol. 8, no. 3, pp. 1274–1283, May 2017.
[10] F. Harrou, B. Taghezouit, and Y. Sun, "Improved kNN-based monitoring schemes for detecting faults in PV systems," *IEEE J. Photovolt.*, vol. 9, no. 3, pp. 811–821, May 2019.
[11] I. M. Karmacharya and R. Gokaraju, "Fault location in ungrounded photovoltaic system using wavelets and ANN," *IEEE Trans. Power Del.*, vol. 33, no. 2, pp. 549–559, Apr. 2018.
[12] Z. Yi and A. H. Etemadi, "Line to line fault detection for photovoltaic arrays based on multiresolution signal decomposition and two stage support vector machine," *IEEE Trans. Ind. Electron.*, vol. 64, no. 11, pp. 8546–8556, Nov. 2017.
[13] B. P. Kumar, S. I. Ganesan, M. J. B. Reddy, and N. Chilakapati, "On-line fault detection and diagnosis in photovoltaic systems using wavelet packets," *IEEE J. Photovolt.*, vol. 8, no. 1, pp. 257–265, Jan. 2018.
[14] J. Sreelakshmy, B. P. Kumar, S. I. Ganesan, and N. Chilakapati, "Identification of faults in PV array using maximal overlap discrete wavelet transform," in *Proc. 20th Nat. Power Syst. Conf.*, 2018, pp. 1–6.
[15] R. Hariharan, M. Chakkarapani, S. I. Ganesan, and N. Chilakapati, "A method to detect photovoltaic array faults and partial shading in PV systems," *IEEE J. Photovolt.*, vol. 6, no. 5, pp. 1278–1285, Sep. 2016.
[16] L. Chen, S. Li, and X. Wang, "Quickest fault detection in photovoltaic systems," *IEEE Trans. Smart Grid*, vol. 9, no. 3, pp. 1835–1847, May 2018.
[17] C. Kuo, J. Chen, S. Chen, C. Kao, H. Yau, and C. Lin, "Photovoltaic energy conversion system fault detection using fractional-order color relation classifier in microdistribution systems," *IEEE Trans. Smart Grid*, vol. 8, no. 3, pp. 1163–1172, May 2017.
[18] P. Jain, J. Poon, J. P. Singh, C. Spanos, S. R. Sanders, and S. K. Panda, "A digital twin approach for fault diagnosis in distributed photovoltaic systems," *IEEE Trans. Power Electron.*, vol. 35, no. 1, pp. 940–956, Jan. 2020.
[19] A. Khoshnami and I. Sadeghkhani, "Sample entropy-based fault detection for photovoltaic arrays," *IET Renew. Power Gener.*, vol. 12, no. 16, pp. 1966–1976, 2018.
[20] K. A. Saleh, A. Hooshyar, E. F. El-Saadany, and H. H. Zeineldin, "Voltage-based protection scheme for faults within utility-scale photovoltaic arrays," *IEEE Trans. Smart Grid*, vol. 9, no. 5, pp. 4367–4382, Sep. 2018.
[21] Y. Hu *et al.*, "Online two-section PV array fault diagnosis with optimized voltage sensor locations," *IEEE Trans. Ind. Electron.*, vol. 62, no. 11, pp. 7237–7246, Nov. 2015.
[22] A. F. Murtaza, M. Bilal, R. Ahmad, and H. A. Sher, "A circuit analysis based fault finding algorithm for photovoltaic array under L-L/L-G faults," *IEEE J. Emerg. Sel. Topics Power Electron.*, Mar. 2019, doi: 10.1109/JESTPE.2019.2904656.
[23] E. D. Aranda, J. A. G. Galan, M. S. de Cardona, and J. M. A. Marquez, "Measuring the I-V curve of PV generators," *IEEE Ind. Electron. Mag.*, vol. 3, no. 3, pp. 4–14, Sep. 2009.
[24] E. Duran, M. Piliougine, M. Sidrach-de-Cardona, J. Galan, J. M. Andujar, "Different methods to obtain the IV curve of PV modules: A review," in *Proc. 33rd IEEE Photovolt. Specialists Conf.*, San Diego, CA, USA, 2008, pp. 1–6.
[25] W. Wang, A. C. Liu, H. S. Chung, R. W. Lau, J. Zhang, and A. W. Lo, "Fault diagnosis of photovoltaic panels using dynamic current-voltage characteristics," *IEEE Trans. Power Electron.*, vol. 31, no. 2, pp. 1588–1599, Feb. 2016.
[26] M. Manjunath, B. V. Reddy, Y. Zhao, and B. Lehman, "Online health monitoring of PV plants," in *Proc. IEEE Energy Convers. Congr. Expo.*, Oct. 2017, pp. 4061–4068.
[27] D. S. Pillai and N. Rajasekar, "An MPPT based sensorless line-line and line-ground fault detection technique for PV systems," *IEEE Trans. Power Electron.*, vol. 34, no. 9, pp. 8646–8659, Sep. 2019.
[28] K. A. Kim, G. Seo, B. Cho, and P. T. Krein, "Photovoltaic hot-spot detection for solar panel substrings using ac parameter characterization," *IEEE Trans. Power Electron.*, vol. 31, no. 2, pp. 1121–1130, Feb. 2016.
[29] "Abb string inverters,pvi-3.0/3.6/4.2-tl-outd," ABB Ltd. [Online]. Available: https://loopsolar.com/datasheet/abb-solar/ABB-solar-string-inverter-PVI-3-4K
[30] "Sun2000 (8KTL-28KTL) PV inverters user manual," Huawei Technologies Co. Ltd., Tech. report. [Online]. Available: https://support.huawei.com/enterprise/en/doc/EDOC1100022053
[31] D. Hamza and K. H. A. Hosani, "Dc-link input EMI filter design in a centralized architecture PV inverter: Impedance approach," in *Proc. IEEE Energy Convers. Congr. Expo.*, Sep. 2014, pp. 4777–4783.
[32] "INVT iMars MG-series grid tied solar inverters user manual," Tech. Rep., Shenzhen INVT Electric Co., Ltd. 2019. [Online]. Available: https://www.invt-solar.com/uploadfiles/2019/02/INVT_MG%200.75-6KW%20user%20manual.pdf
[33] C. Manickam, G. P. Raman, G. R. Raman, S. I. Ganesan, and N. Chilakapati, "Fireworks enriched P&O algorithm for GMPPT and detection of partial shading in PV systems," *IEEE Trans. Power Electron.*, vol. 32, no. 6, pp. 4432–4443, Jun. 2017.
[34] N. Femia, G. Petrone, G. Spagnuolo, and M. Vitell, *Power Electronics and Control Techniques for Maximum Energy Harvesting in Photovoltaic Systems*. Boca Raton, FL, USA: CRC Press, 2013.
[35] M. G. Villalva, J. R. Gazoli, and E. R. Filho, "Comprehensive approach to modeling and simulation of photovoltaic arrays," *IEEE Trans. Power Electron.*, vol. 24, no. 5, pp. 1198–1208, May 2009.
[36] P. Hernday, "Solar I-V curves interpreting trace deviations," in *Solar Pro Magazine*, Aug./Sep. 2014. [Online]. Available: https://www.scribd.com/document/371015917/SolarPro-I-V-Feature-Article-%Hernday
[37] K. Nakayashiki *et al.*, "Engineering solutions and root-cause analysis for light-induced degradation in p-type multicrystalline silicon PERC modules," in *IEEE J. Photovolt.*, vol. 6, no. 4, pp. 860–868, July 2016.
[38] F. Kersten *et al.*, "Degradation of multicrystalline silicon solar cells and modules after illumination at elevated temperature," *Solar Energy Mater. Solar Cells*, vol. 142, pp. 83–86, 2015.
[39] M. Köntges *et al.*, "Performance and reliability of photovoltaic systems, subtask 3.2: Review of failures of photovoltaic modules," Int. Energy Agency, Tech. Rep. IEA-PVPS T13-01:2014, 2014.
[40] S. Pingel *et al.*, "Potential induced degradation of solar cells and panels," in *Proc. 35th IEEE Photovolt. Spec. Conf.*, Jun. 2010, pp. 002817–002822.

Pradeep Kumar Boggarapu (Student Member, IEEE) received the B.Tech. degree in electrical and electronics engineering from K.S.R.M. College of Engineering, Kadapa, India, in 2005, and the M.Tech. degree in power electronics from the B.M.S. College of Engineering, Bangalore, India, in 2008.

From 2009 to 2015, he was with the Department of Electrical and Electronics Engineering, VITS, Proddatur, Andhra Pradesh, India. He is currently a full-time Research Scholar with the National Institute of Technology, Tiruchirappalli, Tamilnadu, India. His research interests include identification of faults, degradation in photovoltaic systems, and power electronics.

Chakkarapani Manickam received the B.Tech. degree in electrical and electronics engineering, the M.Tech. degree in process control and instrumentation, and the Ph.D. degree in electrical and electronics engineering from the National Institute of Technology, Tiruchirappalli, Tamilnadu, India, in 2008, 2010, and 2017, respectively.

He is currently a Senior Assistant Professor with the Department of Electrical and Electronics Engineering, Madanapalle Institute of Technology and Science, Madanapalle, Andhra Pradesh, India. His research interests include digital control systems and applications of power electronics in renewable energy systems.

Brad Lehman (Fellow, IEEE) received the Ph.D.E.E. degree from the Georgia Institute of Technology, Atlanta, GA, USA, in 1992.

He is currently a Professor with the Department of Electrical and Computer Engineering, Northeastern University, Boston, MA, USA. He performs research in power electronics, smart solar energy, LED lighting, battery chargers, and telecommunication power supplies.

Dr. Lehman was the Editor-in-Chief of the IEEE TRANSACTIONS ON POWER ELECTRONICS. He received the 2015 IEEE (PELS) Power Electronics Society Modeling and Control Technical Achievement Award, the 2016 IEEE Standards Medallion, the 2018 IEEE Award for Achievement in Power Electronics Standards, and the 2019 IEEE PELS Harry A. Owen, Jr. Distinguished Service Award. He has been listed in the inaugural edition of the book—*The 300 Best Professors* (Princeton Review, 2012).

Saravana Ilango Ganesan (Senior Member, IEEE) received the B.E. degree from Madras University, Chennai, India, in 2000, the M.E. degree from Bharathithasan University, Tiruchirappalli, India, in 2001, and the Ph.D. degree from the National Institute of Technology, Tiruchirappalli, India, in 2009.

From 2001 to 2004, he was a Lecturer with the Noorul Islam College of Engineering, Kumaracoil, India. He is currently an Associate Professor with the Department of Electrical and Electronics Engineering, National Institute of Technology, Tiruchirappalli, Tamil Nadu, India. His research interests include flexible ac transmission system controllers, digital controllers, and renewable energy systems.

Nagamani Chilakapati (Senior Member, IEEE) received the M.Tech. degree from the Indian Institute of Technology, Kanpur, India, and the Ph.D. degree from the University of Technology, Sydney, NSW, Australia, in 1984 and 2001.

From 1985 to 1991, she was with the Central Power Research Institute, Bangalore, India. Subsequently, she joined the Department of Electrical and Electronics Engineering, National Institute of Technology, Tiruchirappalli, Tamil Nadu, India, where she is currently a Professor. Her research interests include power electronics and drives, renewable energy systems, and flexible ac transmission system controllers.